SCIENCE CHINA
Chemistry

•ARTICLES•

February 2024 Vol.67 No.2: 687–695
https://doi.org/10.1007/s11426-023-1761-8

Divalent anion intercalation and etching-hydrolysis strategies to construct ultra-stable electrodes for seawater splitting

Jiajia Lu[1,2†], Yang Liu[3†] & Han-Pu Liang[1,4,5*]

[1]*Key Laboratory of Biofuels, Qingdao Institute of Bioenergy and Bioprocess Technology, Chinese Academy of Sciences, Qingdao 266101, China;*
[2]*Henan Provincial Key Laboratory of Nanocomposites and Applications, Institute of Nano-Structured Functional Materials, Huanghe Science and Technology College, Zhengzhou 450006, China;*
[3]*School of Materials Science and Engineering, Henan Normal University, Xinxiang 453007, China;*
[4]*Center of Materials Science and Optoelectronics Engineering, University of Chinese Academy of Sciences, Beijing 100049, China;*
[5]*Shandong Energy Institute, Qingdao 266101, China*

Received July 5, 2023; accepted August 17, 2023; published online August 25, 2023

Developing stable electrodes for seawater splitting remains a great challenge due to the detachment of catalysts at a large operating current and severe anode corrosion caused by chlorine. Herein, divalent anion intercalation and etching-hydrolysis strategies are deployed to synthesize the ultra-stable anode, dendritic $Fe(OH)_3$ grown on $Ni(SO_4)_{0.3}(OH)_{1.4}$–$Ni(OH)_2$. Experimental results reveal that the anode exhibits good activity and excellent stability in alkaline simulated seawater. After 500 h, the current density operated at 1.72 V remains 99.5%, about 210 mA cm^{-2}. The outstanding stability originates from the etching-hydrolysis strategy, which strengthens the interaction between the catalyst and the carrier and retards thus the detachment of catalysts at a large current density. Besides, theoretical simulations confirm that the intercalated divalent anions, such as SO_4^{2-} and CO_3^{2-}, can weaken the adsorption strength of chlorine on the surface of catalysts and hinder the coupling and hybridization between chlorine and nickel, which slows down the anode corrosion and improves catalytic stability. Furthermore, the two-electrode system shows the remarkable 95.1% energy efficiency at 2,000 A m^{-2} and outstanding stability in 6 mol L^{-1} KOH + seawater at 80 °C.

seawater splitting, stability, divalent anion intercalation, etching-hydrolysis

Citation: Lu J, Liu Y, Liang HP. Divalent anion intercalation and etching-hydrolysis strategies to construct ultra-stable electrodes for seawater splitting. *Sci China Chem*, 2024, 67: 687–695, https://doi.org/10.1007/s11426-023-1761-8

1 Introduction

The seawater, accounting for more than 96.5% of the earth's water reserves, has been considered as a sustainable energy conversion to replace fresh water for hydrogen production [1–5]. However, much more challenges occur in seawater splitting due to the more complex composition of seawater, usually containing multiple anions (such as Cl^-, SO_4^{2-}, Br^- and HCO_3^-) and cations (such as Na^+, Mg^{2+}, Ca^{2+} and K^+): (1) the increase of local pH at the cathode leads to the precipitation of Mg/Ca hydroxides, blocking electrodes [6–8]; (2) the high concentration of Cl^- at the anode would corrode the anode catalyst or result in the competitive reaction, the oxidation reaction of Cl^- (the Cl_2/HOCl/ClO^- redox couples depending on pH values) [9–13].

To overcome the first issue, researchers usually pretreat the seawater by introducing alkali to remove most of the above precipitation. In the case of the second issue, the competitive reaction and the corrosion of catalysts caused by Cl^- is un-

†These authors contributed equally to this work.
*Corresponding author (email: lianghp@qibebt.ac.cn)

avoidable at the anode under a high potential. The oxidation reaction of Cl^- (ClOR, $Cl^-+2OH^-\rightarrow ClO^-+H_2O+2e^-$) and the oxygen evolution reaction (OER) are competitive in alkaline seawater [14]. Their difference in the equilibrium potential is approximately 490 mV (E^0_{ClOR}–E^0_{OER}) [15,16]. Therefore, a 100% OER selectivity can be obtained when the overpotential of oxygen evolution is at or below 490 mV [3,17]. However, it is very challenging to meet the required high current density in the industry at such low overpotentials [17–19].

Recently, theoretical and experimental results show that the oxyhydroxides of Ni and Fe possess not only good OER activity but also better OER selectivity than the commercial IrO_2 because of the weak Cl^- adsorption on the surface of catalysts, which impedes the subsequent step of ClOR [3,15]. Nevertheless, the oxyhydroxides of Ni and Fe suffer from the severe corrosion caused by Cl^-. Thus, a passivation layer strategy is proposed to resist the chlorine corrosion. For instance, Dai *et al*. [15] reported a multilayer NiFe/NiS_x–Ni foam anode, in which the underlying NiS_x layer could be oxidized to polyatomic sulfate, repelling the Cl^- in seawater. Further, Chen *et al*. [10] found that the SO_4^{2-} adsorbed on the NiFe-layered double hydroxide can repel the Cl^- by electrostatic reaction and improve corrosion resistance. Despite the significant progress on catalysts to repel Cl^-, the intercalation of anions in the crystal lattice of catalysts to resist chlorine corrosion has not been reported yet. Additionally, the stability of electrode structure, a common problem for all catalysts, still faces tremendous challenges at a large current density due to the weak interaction between the catalysts and the carrier by the traditional method of introducing OH^- or alkaline precipitants, which usually leads to the detachment of catalysts and the decay of catalytic activity [20–25]. Therefore, developing highly active electrodes with the high corrosion resistance to Cl^- and stable structure still is a great challenge for seawater splitting.

Herein, we report divalent anion intercalation and etching-hydrolysis strategies to construct an ultra-stable anode, dendritic $Fe(OH)_3$ grown on $Ni(SO_4)_{0.3}(OH)_{1.4}$–$Ni(OH)_2$, for seawater splitting. The intercalated divalent anions can decrease the adsorption strength of chlorine ions on the surface of hydroxides and hence alleviate the chlorine corrosion. In addition, the etching-hydrolysis strategy could enhance the interaction between the catalyst and the carrier, thereby improving the structural stability of electrodes. Benefiting from the combination of the above two advantages, the anode shows outstanding stability in alkaline simulated seawater. The current density remains 99.5%, about 210 mA cm^{-2}, at 1.72 V after 500 h. When the anode is paired with the previously reported cathode, the encapsulated Ni nanoparticles in the incomplete graphite layer anchored on nanobelts consisting of Ni oxide and Mo oxide (IG@Ni–$NiMoO_x$), [26] the two-electrode system also exhibits outstanding activity and stability in 6 mol L^{-1} KOH + seawater at 80 °C.

2 Results and discussion

2.1 Synthesis and structural characterization

Schematic illustration for the synthesis of $Fe(OH)_3$–$Ni(SO_4)_{0.3}(OH)_{1.4}$–$Ni(OH)_2$ is shown in Figure 1a. Firstly, the $Ni(SO_4)_{0.3}(OH)_{1.4}$–$Ni(OH)_2$ grows on a piece of Ni foam and the growth mechanism is clarified by our previous report [26]. The nanobelt-like $Ni(SO_4)_{0.3}(OH)_{1.4}$ fabricated at 160 °C for 12 h is observed in Figure 1b and Figure S1.

Secondly, the $Fe(OH)_3$, which possesses a lower solubility product constant (K_{sp}, 4.0×10^{-38}) than $Ni(SO_4)_{0.3}(OH)_{1.4}$ ($>2.0\times10^{-15}$), can grow spontaneously on $Ni(SO_4)_{0.3}(OH)_{1.4}$ nanobelts at ambient temperature through an etching-hydrolysis strategy. Therefore, the surface of $Ni(SO_4)_{0.3}(OH)_{1.4}$ nanobelts could be partly etched in the acidic $Fe_2(SO_4)_3$ solution and then the Fe^{3+} is hydrolyzed to form dendritic $Fe(OH)_3$ on $Ni(SO_4)_{0.3}(OH)_{1.4}$–$Ni(OH)_2$, named $Fe(OH)_3$–$Ni(SO_4)_{0.3}(OH)_{1.4}$–$Ni(OH)_2$, as evidenced from the SEM images (Figure 1c, d and Figure S2a) and transmission electron microscopy (TEM) images in Figure 2a, b. The distribution and content of elements are further identified by corresponding energy-dispersive spectroscopy (EDS) mapping images and spectra (Figure S2b, Table S1 and Figure 2d, e). Although there are no diffraction peak correlated to $Fe(OH)_3$ from the XRD pattern in Figure 1e, both the different crystal facets of $Fe(OH)_3$ in the high-resolution TEM (HRTEM) image in Figure 2c and the Raman spectra in Figure S3, from which the broad band at 695 cm^{-1} presents a characteristic peak for the $Fe(OH)_3$, suggest the presence of $Fe(OH)_3$ [27,28]. Additionally, the presence of intercalated divalent anions such as SO_4^{2-} and CO_3^{2-} is confirmed by the X-ray photoelectron spectroscopy (XPS) spectra in Figure 1f, g, Raman spectra in Figure S3 and infrared spectra in Figure S4. These results indicate that the $Fe(OH)_3$–$Ni(SO_4)_{0.3}(OH)_{1.4}$–$Ni(OH)_2$ with divalent anion intercalations has been successfully fabricated on a Ni foam.

2.2 Evaluation towards electrochemical oxygen evolution

After the anodic activation of $Fe(OH)_3$–$Ni(SO_4)_{0.3}(OH)_{1.4}$–$Ni(OH)_2$ at 100 mA cm^{-2} for 16 h in 1 mol L^{-1} KOH, similar OER activity in 1 mol L^{-1} KOH, 1 mol L^{-1} KOH + 0.5 mol L^{-1} NaCl, and 1 mol L^{-1} KOH + seawater is observed in Figure 3a. The slight difference may be attributed to the different solution resistance, which is affected by the concentration of ions and the distance between electrodes in the electrolyte. After ohmic *iR* compensation, the overpotential of $Fe(OH)_3$–$Ni(SO_4)_{0.3}(OH)_{1.4}$–$Ni(OH)_2$ to drive 100 mA cm^{-2} is 268 mV in 1 mol L^{-1} KOH + 0.5 mol L^{-1}

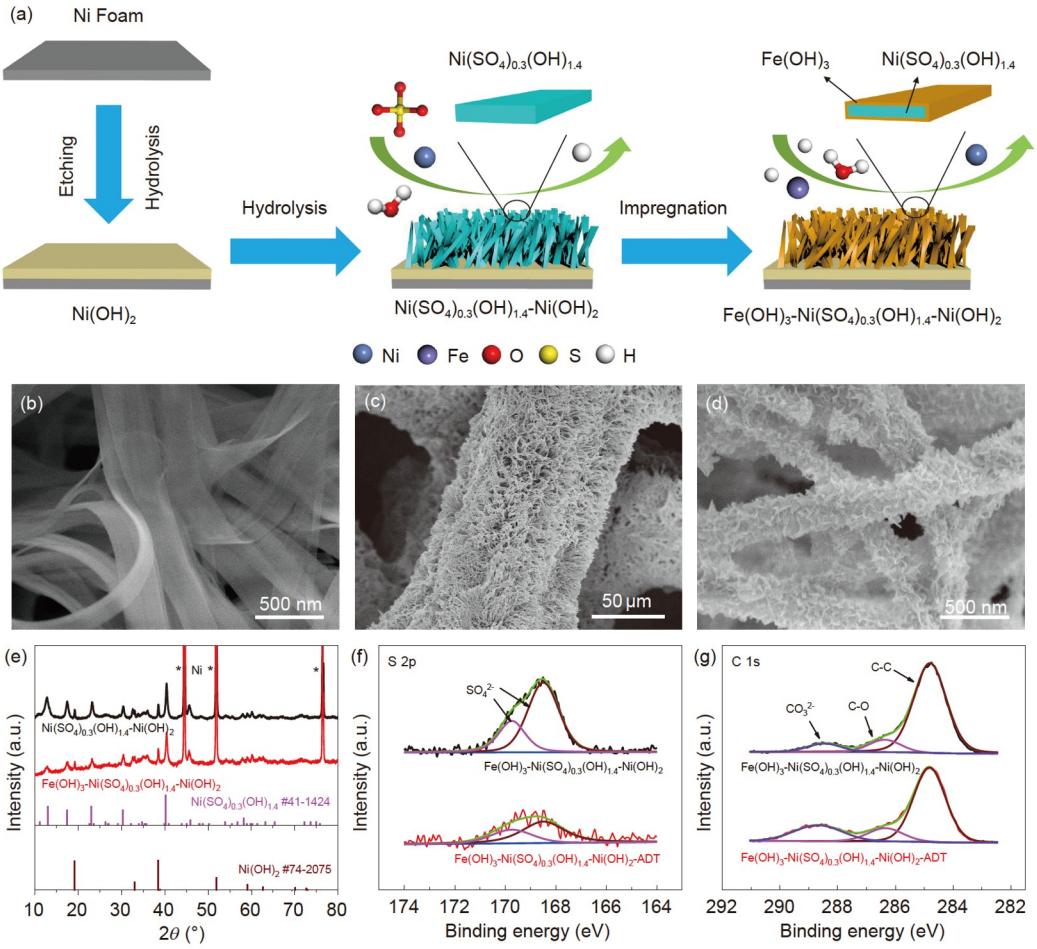

Figure 1 (a) Schematic illustration for the synthesis of $Fe(OH)_3$–$Ni(SO_4)_{0.3}(OH)_{1.4}$–$Ni(OH)_2$ anode. (b) A SEM image of $Ni(SO_4)_{0.3}(OH)_{1.4}$–$Ni(OH)_2$. (c, d) SEM images of $Fe(OH)_3$–$Ni(SO_4)_{0.3}(OH)_{1.4}$–$Ni(OH)_2$. (e) XRD patterns of $Ni(SO_4)_{0.3}(OH)_{1.4}$–$Ni(OH)_2$ and $Fe(OH)_3$–$Ni(SO_4)_{0.3}(OH)_{1.4}$–$Ni(OH)_2$. (f, g) High-resolution XPS spectra of S 2p and C 1s of $Fe(OH)_3$–$Ni(SO_4)_{0.3}(OH)_{1.4}$–$Ni(OH)_2$ activated in 1 mol L^{-1} KOH under 100 mA cm^{-2} for 16 h and after accelerated durability test (ADT) in 1 mol L^{-1} KOH + 0.5 mol L^{-1} NaCl at 1.72 V for 500 h (color online).

NaCl aqueous solution (Figure 3b). Compared with as-synthesized catalysts in Figure 3d and reported catalysts in Table S3, the $Fe(OH)_3$–$Ni(SO_4)_{0.3}(OH)_{1.4}$–$Ni(OH)_2$ shows better catalytic activity. Furthermore, it is obvious that the Tafel slopes of $Fe(OH)_3$–$Ni(SO_4)_{0.3}(OH)_{1.4}$–$Ni(OH)_2$ and $Fe(OH)_3$–$Ni(OH)_2$ in Figure 3e are lower than that of other as-synthesized catalysts in the absence of Fe, suggesting that the presence of Fe enhances the catalytic kinetics of the reaction. Therefore, good catalytic activity could originate from the incorporation of Fe, forming the α-FeOOH on $Ni(SO_4)_{0.3}$-$(OH)_{1.4}$ and β-$Ni(OH)_2$ demonstrated by the *in-situ* Raman spectra and XPS spectra. As shown from the Raman spectra in Figure 3c, when the potential is increased from 1.12 to 1.52 V, the emerging bands at 303, 377 and 443 cm^{-1} indicate the formation of α-FeOOH and β-$Ni(OH)_2$ [29–31]. However, the Ni–O vibrations at 474 and 554 cm^{-1} of NiOOH that is usually converted from the $Ni(OH)_2$ at high potentials are absent, which could be tentatively attributed to the effect of intercalated SO_4^{2-}. Additionally, from the XPS spectra of $Fe(OH)_3$–$Ni(SO_4)_{0.3}(OH)_{1.4}$–$Ni(OH)_2$ in Figure S5, three peaks at 529.58, 531.23 and 532.93 eV related to the O^{2-}, –OH and other adsorbed species such as H_2O are observed, which indicates that the FeOOH presents on the surface of the catalyst [31–36].

In practical applications, the solution resistance is inevitable and the catalytic performance of all catalysts without *iR* compensation thus is presented in this work. Additionally, in order to avoid the competitive reaction of ClOR, the overpotential of OER needs to be lower than the difference in the equilibrium potential (E^0_{ClOR}–E^0_{OER}=490 mV). Consequently, the operating potential was held at 1.72 V to evaluate OER stability. The $Fe(OH)_3$–$Ni(SO_4)_{0.3}(OH)_{1.4}$–$Ni(OH)_2$ shows excellent stability. The current density remains 99.5% at 1.72 V after 500 h in 1 mol L^{-1} KOH + 0.5 mol L^{-1} NaCl aqueous solution (Figure 3f) and the OER polarization curve after ADT almost coincides with that before ADT (Figure 3b). Compared with those catalysts reported previously in Figure 3h, the operating time of $Fe(OH)_3$–$Ni(SO_4)_{0.3}(OH)_{1.4}$–$Ni(OH)_2$ exhibits significant advantages.

The excellent stability could be ascribed to the stable

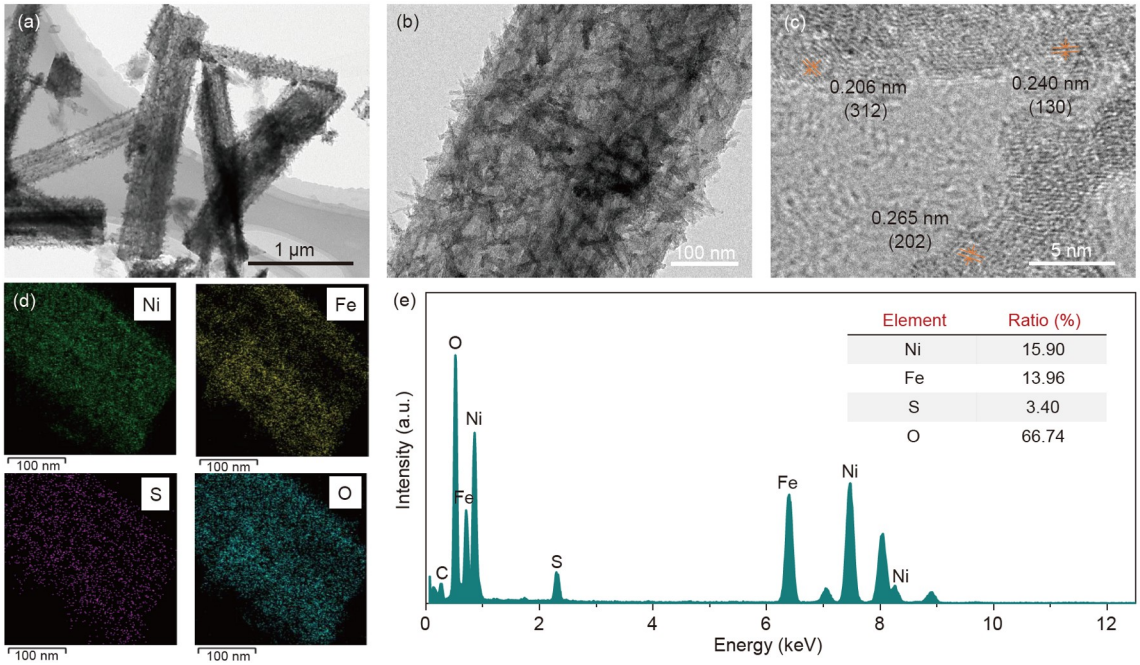

Figure 2 (a, b) TEM and (c) HRTEM images of $Fe(OH)_3$–$Ni(SO_4)_{0.3}(OH)_{1.4}$–$Ni(OH)_2$. The corresponding EDS mapping images (d) and spectra (e) of Ni, Fe, S and O. The inset shows their atomic ratios (color online).

physical structure of catalysts obtained through the etching-hydrolysis strategy, as well as the intercalated divalent anions. The stable physical structure of catalysts can be demonstrated by SEM images, XRD patterns, XPS spectra and ICP. After ADT, the slight change of dendritic $Fe(OH)_3$–$Ni(SO_4)_{0.3}(OH)_{1.4}$–$Ni(OH)_2$ nanobelts is observed from SEM images (Figure S6) and the catalyst still firmly stays on the surface of the Ni foam. Furthermore, as evidenced from the XRD pattern of $Fe(OH)_3$–$Ni(SO_4)_{0.3}(OH)_{1.4}$–$Ni(OH)_2$ after ADT in Figure S7, the diffraction peaks are similar to that before ADT. In addition, XPS spectra show that the atomic ratio of Ni to Fe is 1.2 to 1 after ADT in Table S2. The results from ICP display that the weight of Ni and Fe in catalysts after ADT decreases by 27.2% and 21.5%, as shown in Table S4. It indicates that the atomic ratio of Ni to Fe in catalysts before ADT is similar to that after ADT, which is different from the results of XPS because XPS mainly shows the composition of the catalyst at the surface of 3 to 10 nm. Overall, these results indicate that large amounts of Fe (oxy) hydroxides are still on the surface of $Ni(SO_4)_{0.3}(OH)_{1.4}$–$Ni(OH)_2$ after ADT. Therefore, the remarkable stability of the electrode seems to benefit from the etching-hydrolysis methodology, which greatly enhances the interaction between the catalyst and the Ni foam and makes them as a whole electrode. This is obviously different from common catalysts synthesized by introducing OH^- or alkaline precipitants, which weakens the interaction between the hydroxide and the Ni foam, leading to the detachment of catalysts from the substrate after the sonication or catalysis.

Additionally, these intercalated divalent anions can weaken the adsorption strength of Cl^- and alleviate corrosion of the underlying structure. Herein, these intercalated SO_4^{2-} and CO_3^{2-} anions are confirmed by the infrared spectra, Raman spectra and high-resolution XPS spectra. As shown in the infrared spectra of Figure S4, the asymmetric stretching mode (ν_3) of SO_4^{2-} at 1,098 cm^{-1} is observed in the $Fe(OH)_3$–$Ni(SO_4)_{0.3}(OH)_{1.4}$–$Ni(OH)_2$. When the $Fe(OH)_3$–$Ni(SO_4)_{0.3}(OH)_{1.4}$–$Ni(OH)_2$ is activated in 1 mol L^{-1} KOH under 100 mA cm^{-2} for 16 h, the stretching mode (ν_3) of CO_3^{2-} at 1,362 cm^{-1} occurs [43]. Furthermore, Figure S3 shows that the Raman band at 980 cm^{-1} is assigned to the symmetric stretching vibration of SO_4^{2-} [44]. The CO_3^{2-} is identified by the presence of asymmetric stretching vibrations at 1,350 cm^{-1} [45,46]. After ADT, the Raman bands at 980 and 1,350 cm^{-1} display similar peaks, which implies that these intercalated SO_4^{2-} and CO_3^{2-} anions are still in catalysts. Further evidence for the presence of these anions is obtained from XPS spectra in Figure 1f, g. Interestingly, the content of SO_4^{2-} on the surface of catalysts decreases after ADT, whereas the content of CO_3^{2-} increases. This phenomenon is due to the difference of binding energies of some interlayer anions (CO_3^{2-}>SO_4^{2-}>OH^-) in $Ni(OH)_2$ [47,48], resulting in the fact that part of SO_4^{2-} is replaced by CO_3^{2-}, which is derived from the reaction between the CO_2 in air and the OH^- in solution. In addition, the Cl element in the $Fe(OH)_3$–$Ni(SO_4)_{0.3}(OH)_{1.4}$–$Ni(OH)_2$ anode before and after ADT is also detected by XPS spectra in Figure S8. The results show that the negligible content of Cl in the anode is similar before and after ADT, which demonstrates that the designed anode can effectively prevent the adsorption of Cl^-

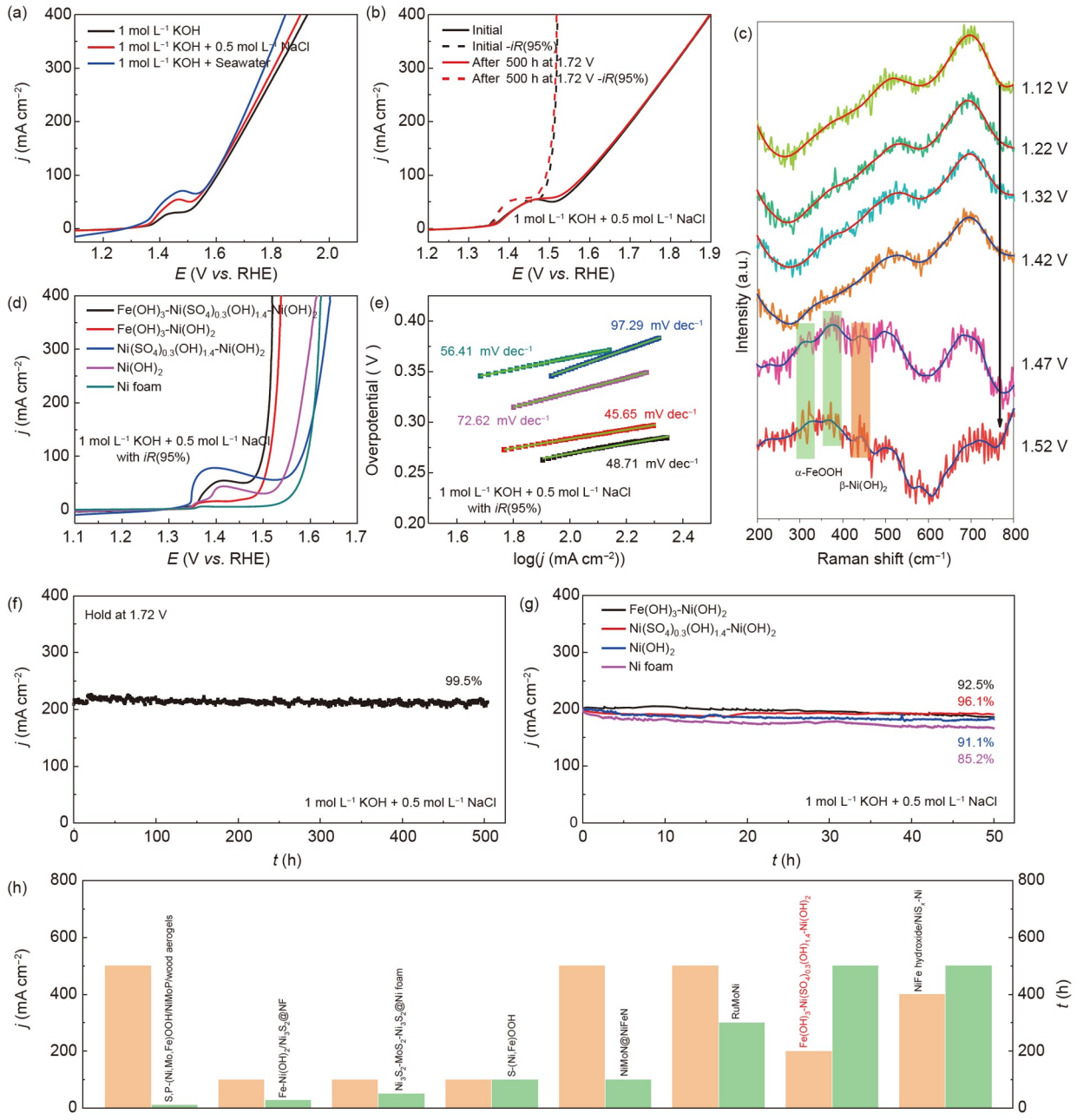

Figure 3 (a) OER polarization curves of $Fe(OH)_3$–$Ni(SO_4)_{0.3}(OH)_{1.4}$–$Ni(OH)_2$ in 1 mol L^{-1} KOH (resistance 1.1 Ω), 1 mol L^{-1} KOH + 0.5 mol L^{-1} NaCl (resistance 1.0 Ω) and 1 mol L^{-1} KOH + seawater (resistance 0.9 Ω). (b) Polarization curves of $Fe(OH)_3$–$Ni(SO_4)_{0.3}(OH)_{1.4}$–$Ni(OH)_2$ before and after ADT in 1 mol L^{-1} KOH + 0.5 mol L^{-1} NaCl at 1.72 V for 500 h. (c) *In-situ* Raman spectra of $Fe(OH)_3$–$Ni(SO_4)_{0.3}(OH)_{1.4}$–$Ni(OH)_2$ as a function of potentials (*vs.* RHE) during an oxidation sweep in 1 mol L^{-1} KOH + 0.5 mol L^{-1} NaCl. (d) Polarization curves and (e) Tafel plots of all the as-synthesized catalysts in 1 mol L^{-1} KOH + 0.5 mol L^{-1} NaCl. Durability evaluation by the chronoamperometry for (f) $Fe(OH)_3$–$Ni(SO_4)_{0.3}(OH)_{1.4}$–$Ni(OH)_2$ (at 1.720 V) and (g) other samples for comparison, $Fe(OH)_3$–$Ni(OH)_2$ (at 1.739 V), $Ni(SO_4)_{0.3}(OH)_{1.4}$–$Ni(OH)_2$ (at 1.844 V), $Ni(OH)_2$ (at 1.814 V) and Ni foam (at 1.814 V) in 1 mol L^{-1} KOH + 0.5 mol L^{-1} NaCl. (h) The current density and operating time of $Fe(OH)_3$–$Ni(SO_4)_{0.3}(OH)_{1.4}$–$Ni(OH)_2$ in alkaline simulated seawater, compared with those catalysts reported previously [15,37–42] (color online).

and improve the catalytic stability.

To further clarify the effect of divalent anions on the catalytic stability, experimental comparisons and theoretical calculations have been conducted. In the control experiments, the $Ni(OH)_2$ (PDF#74-2075, Figure S9) and the $Fe(OH)_3$ grown on $Ni(OH)_2$, named $Fe(OH)_3$–$Ni(OH)_2$, were also synthesized. Subsequently, $Fe(OH)_3$–$Ni(OH)_2$, $Ni(SO_4)_{0.3}(OH)_{1.4}$–$Ni(OH)_2$, $Ni(OH)_2$ and Ni foam were systematically assessed in 1 mol L^{-1} KOH + 0.5 mol L^{-1} NaCl by the chronoamperometry and the chronoamperometric curves are compared in Figure 3g. The $Fe(OH)_3$–$Ni(OH)_2$ exhibits similar catalytic activity to $Fe(OH)_3$–

$Ni(SO_4)_{0.3}(OH)_{1.4}$–$Ni(OH)_2$, while its current density after 50 h shows an obvious decline and only remains 92.5%, lower than that of the $Fe(OH)_3$–$Ni(SO_4)_{0.3}(OH)_{1.4}$–$Ni(OH)_2$ (99.5%) after 500 h. Additionally, the $Ni(OH)_2$ also shows poorer stability than the $Ni(SO_4)_{0.3}(OH)_{1.4}$–$Ni(OH)_2$. The current density of Ni foam decreases linearly and it is found that the Ni foam is significantly corroded. According to the above results, it is rationally speculated that the intercalated SO_4^{2-} anions are responsible for the stability of catalysts.

2.3 Theoretical understanding of the anti-chlorine corrosion

Density functional theory (DFT) calculations were performed by constructing the Ni (111) and $Ni(OH)_2$ (001) models, as well as $Ni(OH)_2$ (001) models intercalated by SO_4^{2-} or CO_3^{2-} anions, which were named Ni, $Ni(OH)_2$, $Ni(OH)_2$_SO_4^{2-}, $Ni(OH)_2$_CO_3^{2-} and $Ni(OH)_2$_SO_4^{2-}_CO_3^{2-} in Figure 4a and Figure S10, for convenience. It is well known that chlorine corrosion is closely related to the adsorption energy of Cl (E_{ad}) on the surface of models [3]. Consequently, the E_{ad} can be used as a descriptor to estimate the resistance of chlorine corrosion, for which a model that gives higher E_{ad} is considered as a potential material to resist the chlorine corrosion. In this work, E_{ad} calculations on the top site of Ni for all models were carried out to evaluate the chlorine corrosion as shown in Figure 4b. The results reveal that the E_{ad} values for the Ni, $Ni(OH)_2$, $Ni(OH)_2$_SO_4^{2-}, $Ni(OH)_2$_CO_3^{2-} and $Ni(OH)_2$_SO_4^{2-}_CO_3^{2-} models are −3.034, −0.795, −0.632, −0.491 and −0.526 eV, respectively. Ob-

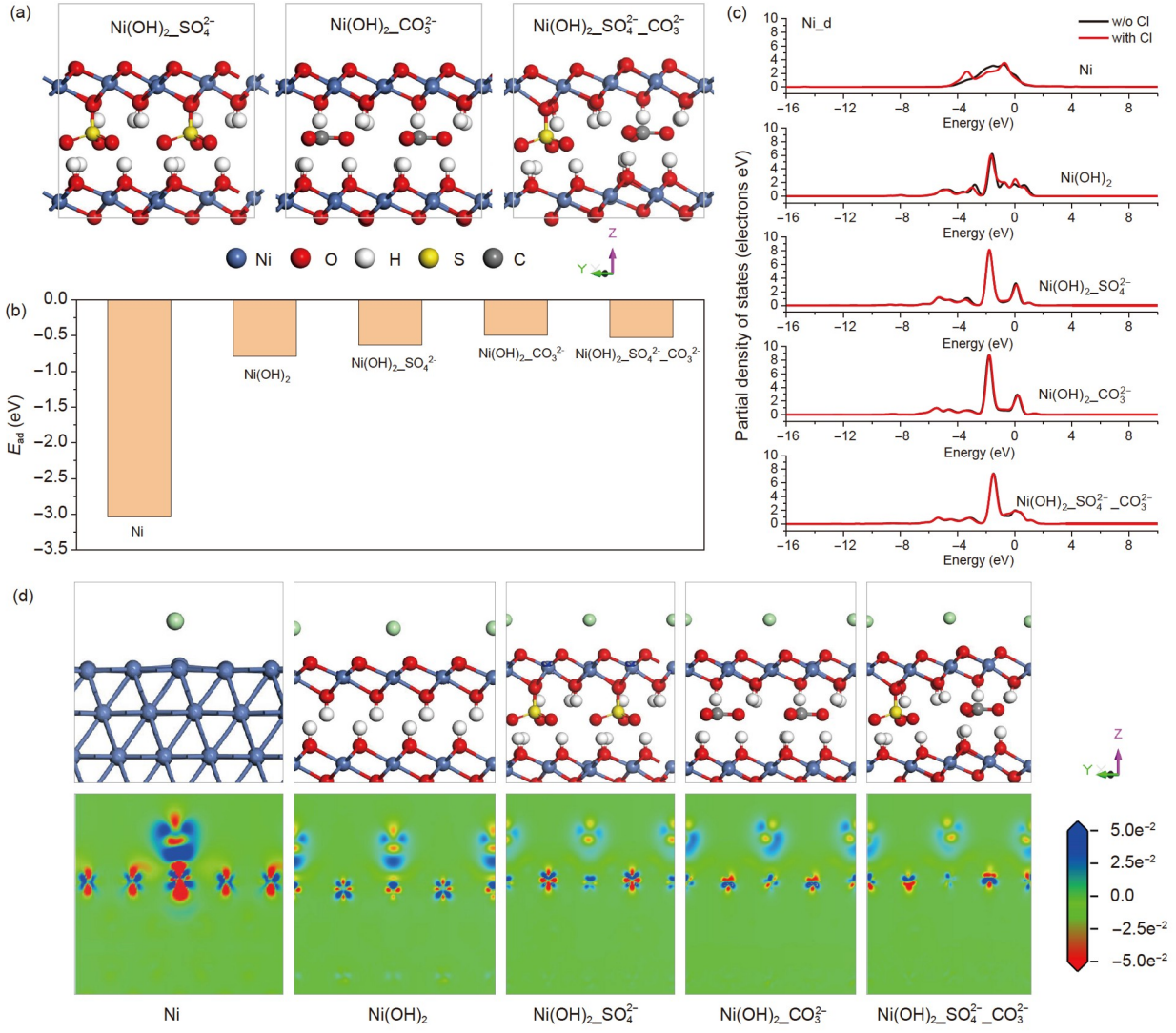

Figure 4 (a) The theoretical models of $Ni(OH)_2$ intercalated by the divalent anions (such as SO_4^{2-} and CO_3^{2-}). (b) The adsorption energy of Cl (E_{ad}) on the Ni (111), $Ni(OH)_2$ (001), $Ni(OH)_2$_SO_4^{2-} (001), $Ni(OH)_2$_CO_3^{2-} (001) and $Ni(OH)_2$_SO_4^{2-}_CO_3^{2-} (001) surfaces, and (c) the partial density of states for Ni in these models with or without Cl. (d) The charge density difference of the all models, where the blue and red areas represent the high and low electron densities (side views of the adsorption sites). Note that the blue, red, yellow, gray, white and cyan spheres denote Ni, O, S, C, H and Cl atoms, respectively (color online).

viously, the Ni exhibits the lowest E_{ad} value among these models, which indicates that the surface of Ni may lead to more severe chlorine corrosion. It is consistent with electrochemical results in Figure 3g, where the current density of the Ni foam decreases linearly and the Ni foam is found to be significantly corroded or even broken. However, the $Ni(OH)_2\_SO_4^{2-}$, $Ni(OH)_2\_CO_3^{2-}$ and $Ni(OH)_2\_SO_4^{2-}\_CO_3^{2-}$ present the higher E_{ad} value compared with the $Ni(OH)_2$ and Ni. It suggests that the adsorption strength of Cl is weak on the surfaces of $Ni(OH)_2\_SO_4^{2-}$, $Ni(OH)_2\_CO_3^{2-}$ and $Ni(OH)_2\_SO_4^{2-}\_CO_3^{2-}$, which effectively alleviates the chlorine corrosion. This result can also be supported by experimental data where the $Ni(SO_4)_{0.3}(OH)_{1.4}$–$Ni(OH)_2$ possesses the higher stability than the others, as shown in Figure 3g.

The partial density of states of Ni and the charge density difference for all models were also calculated in Figures 4c, d. For the Ni and $Ni(OH)_2$ models, the *d*-band of Ni before and after Cl adsorption is obviously different as shown in Figure 4c, which indicates the coupling and hybridization between Ni and Cl after Cl adsorption. Besides, the interaction between Ni and Cl was also confirmed by charge density difference. Figure 4d shows that the blue and red area around atoms represents the high and low electron densities, and the electron transfer is from red to blue areas. Therefore, the electron transfer of the above two models occurs from Ni to Cl. But for the $Ni(OH)_2\_SO_4^{2-}$, $Ni(OH)_2\_CO_3^{2-}$ and $Ni(OH)_2\_SO_4^{2-}\_CO_3^{2-}$ models, as shown in Figure 4c, the *d*-band of Ni after the Cl adsorption is similar to that without the Cl adsorption and no apparent electron transfer is observed in the charge density difference. The coupling and hybridization between Ni and Cl thus may not occur in these models intercalated by divalent anions, which leads to the higher corrosion resistance and outstanding stability of $Fe(OH)_3$–$Ni(SO_4)_{0.3}(OH)_{1.4}$–$Ni(OH)_2$.

2.4 Seawater splitting of the two-electrode system

The $Fe(OH)_3$–$Ni(SO_4)_{0.3}(OH)_{1.4}$–$Ni(OH)_2$ anode was then paired with the IG@Ni–$NiMoO_x$. As shown in Figure 5, the performance of two electrodes ($Fe(OH)_3$–$Ni(SO_4)_{0.3}(OH)_{1.4}$–$Ni(OH)_2$ as the anode, IG@Ni–$NiMoO_x$ as the cathode) for water splitting was evaluated in 6 mol L^{-1} KOH + seawater at 80 °C. From Figure 5a, the polarization curve of the two-electrode system exhibits the outstanding catalytic activity without ohmic *iR* compensation. The voltages of water splitting to drive 100 and 200 mA cm^{-2} are only 1.461 and 1.558 V. Compared with other reported catalysts, [15,49–51] the above two-electrode system shows better catalytic activity for seawater splitting. In addition, the energy required to produce hydrogen per cubic meter at different current densities and the corresponding energy efficiency were recorded in Figure 5b. Herein, the calorific value of hydrogen

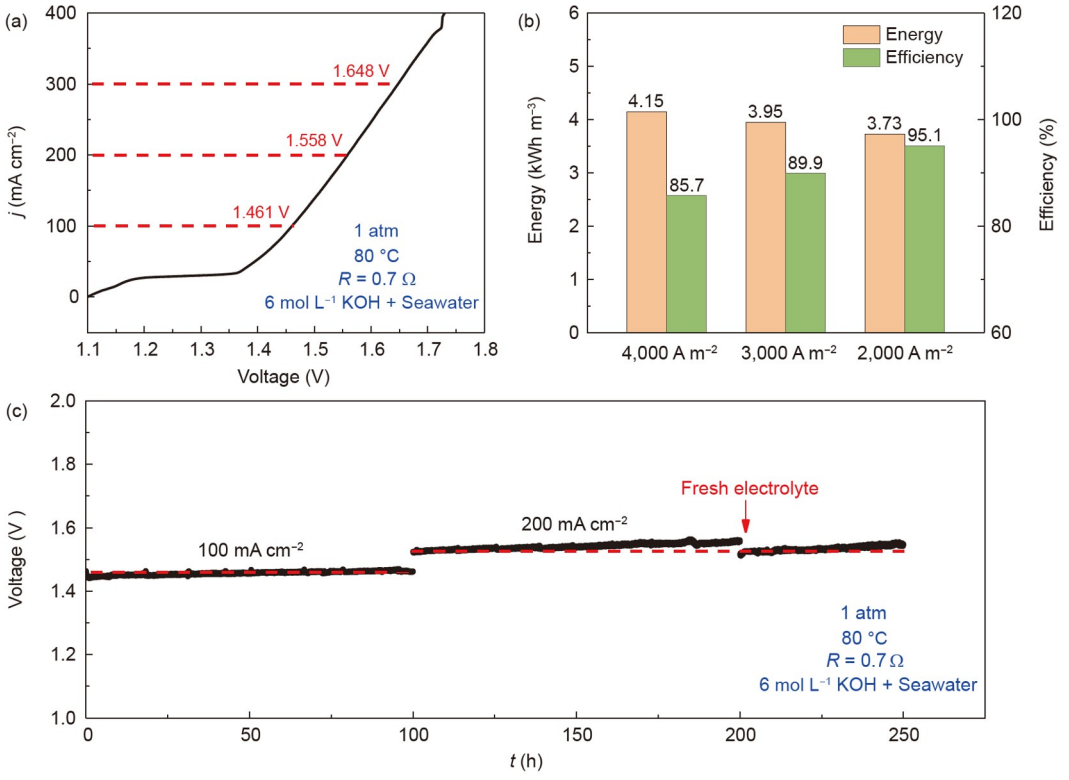

Figure 5 (a) The polarization curve of the two-electrode system ($Fe(OH)_3$–$Ni(SO_4)_{0.3}(OH)_{1.4}$–$Ni(OH)_2$ as the anode, IG@Ni–$NiMoO_x$ as the cathode) without ohmic *iR* compensation. (b) The energy is required to produce hydrogen per cubic meter at different current densities and the corresponding energy efficiency. (c) Durability evaluation of two electrodes by the chronopotentiometry at 100 and 200 mA cm^{-2} for 250 h (color online).

is adopted as the energy of hydrogen. The results display that the energy efficiency operated at 2,000 A m^{-2} is 95.1%. Even at 4,000 A m^{-2}, the energy efficiency still reaches 85.7%, which exceeds the energy efficiency (70%–80%) of the commercial electrolysis system. Subsequently, a chronopotentiometry operated at 100 and 200 mA cm^{-2} for 250 h was used to evaluate the catalytic stability. Figure 5c shows that the voltage of water splitting at 100 mA cm^{-2} remains almost constant and the voltage of water splitting at 200 mA cm^{-2} increases slightly after 100 h. Interestingly, the voltage changes to the initial value after replacing the electrolyte, because the high temperature and a large number of bubbles accelerate the loss of electrolytes.

3 Conclusions

In summary, we have developed divalent anion intercalation and etching-hydrolysis strategies to fabricate the $Fe(OH)_3$–$Ni(SO_4)_{0.3}(OH)_{1.4}$–$Ni(OH)_2$ anode with good OER activity and outstanding stability in 1 mol L^{-1} KOH + 0.5 mol L^{-1} NaCl. The current density remained 99.5%, about 210 mA cm^{-2}, at 1.72 V after 500 h. The good catalytic activity is due to these highly active phases such as the α-FeOOH on $Ni(SO_4)_{0.3}(OH)_{1.4}$ and β-$Ni(OH)_2$ confirmed by *in-situ* Raman spectra. The excellent stability benefits from the etching-hydrolysis strategy that constructs a stable physical structure to resist the damage of the large current to catalysts. Besides, theoretical simulations and control experiments showed that the intercalated divalent anions such as SO_4^{2-} and CO_3^{2-} can weaken the adsorption strength of Cl^- and enhance the corrosion resistance to Cl^- at the anode, and thus improve the OER stability. Furthermore, the anode was paired with the IG@Ni–$NiMoO_x$ cathode and also exhibited the remarkable energy efficiency at different current densities and extended the stability over 250 h in 6 mol L^{-1} KOH + seawater at 80 °C. More importantly, the aforementioned etching-hydrolysis and divalent anion intercalation strategies are very significant in promoting the fundamental study of seawater splitting as well as their practical applications.

Acknowledgements This work was supported from the China Postdoctoral Science Foundation (2020M682250), the Natural Science Foundation of Shandong Province (ZR2022QB062, ZR2021MB070) and the DNL Cooperation Fund, CAS (DNL202010). Additionally, we also thank the Shanxi Supercomputing Center of China for its support with the calculations.

Conflict of interest The authors declare no conflict of interest.

Supporting information The supporting information is available online at chem.scichina.com and link.springer.com/journal/11426. The supporting materials are published as submitted, without typesetting or editing. The responsibility for scientific accuracy and content remains entirely with the authors.

1 Dresp S, Dionigi F, Klingenhof M, Strasser P. *ACS Energy Lett*, 2019, 4: 933–942
2 Juodkazytė J, Šebeka B, Savickaja I, Petrulevičienė M, Butkutė S, Jasulaitienė V, Selskis A, Ramanauskas R. *Int J Hydrogen Energy*, 2019, 44: 5929–5939
3 Li J, Liu Y, Chen H, Zhang Z, Zou X. *Adv Funct Mater*, 2021, 31: 2101820
4 Jin H, Liu X, Vasileff A, Jiao Y, Zhao Y, Zheng Y, Qiao SZ. *ACS Nano*, 2018, 12: 12761–12769
5 Wang H, Cui M, Fu G, Zhang J, Ding X, Azaceta I, Bugnet M, Kepaptsoglou DM, Lazarov VK, de la Peña O'Shea VA, Oropeza FE, Zhang KHL. *Sci China Chem*, 2022, 65: 1885–1894
6 Tong W, Forster M, Dionigi F, Dresp S, Erami RS, Strasser P, Cowan AJ, Farràs P. *Nat Energy*, 2021, 6: 935
7 Kirk D, Ledas A. *Int J Hydrogen Energy*, 1982, 7: 925–932
8 Bennett J. *Int J Hydrogen Energy*, 1980, 5: 401–408
9 Wang C, Shang H, Jin L, Xu H, Du Y. *Nanoscale*, 2021, 13: 7897–7912
10 Ma T, Xu W, Li B, Chen X, Zhao J, Wan S, Jiang K, Zhang S, Wang Z, Tian Z, Lu Z, Chen L. *Angew Chem Int Ed*, 2021, 60: 22740–22744
11 Zhong H, Wang J, Meng F, Zhang X. *Angew Chem Int Ed*, 2016, 55: 9937–9941
12 Xie H, Zhao Z, Liu T, Wu Y, Lan C, Jiang W, Zhu L, Wang Y, Yang D, Shao Z. *Nature*, 2022, 612: 673–678
13 Shi H, Wang T, Liu J, Chen W, Li S, Liang J, Liu S, Liu X, Cai Z, Wang C, Su D, Huang Y, Elbaz L, Li Q. *Nat Commun*, 2023, 14: 3934
14 Yu H, Wan J, Goodsite M, Jin H. *One Earth*, 2023, 6: 267–277
15 Kuang Y, Kenney MJ, Meng Y, Hung WH, Liu Y, Huang JE, Prasanna R, Li P, Li Y, Wang L, Lin MC, McGehee MD, Sun X, Dai H. *Proc Natl Acad Sci USA*, 2019, 116: 6624–6629
16 Khatun S, Hirani H, Roy P. *J Mater Chem A*, 2021, 9: 74–86
17 Dionigi F, Reier T, Pawolek Z, Gliech M, Strasser P. *ChemSusChem*, 2016, 9: 962–972
18 Zou X, Liu Y, Li GD, Wu Y, Liu DP, Li W, Li HW, Wang D, Zhang Y, Zou X. *Adv Mater*, 2017, 29: 1700404
19 Zhu L, Lin H, Li Y, Liao F, Lifshitz Y, Sheng M, Lee ST, Shao M. *Nat Commun*, 2016, 7: 12272
20 Lee J, Jung H, Park YS, Kwon N, Woo S, Selvam NCS, Han GS, Jung HS, Yoo PJ, Choi SM, Han JW, Lim B. *Appl Catal B-Environ*, 2021, 294: 120246
21 Qian G, Yu G, Lu J, Luo L, Wang T, Zhang C, Ku R, Yin S, Chen W, Mu S. *J Mater Chem A*, 2020, 8: 14545–14554
22 Li Z, Wang K, Tan X, Liu X, Wang G, Xie G, Jiang L. *Chem Eng J*, 2021, 424: 130390
23 Zhang X, Chen N, Wang Y, Wu G, Du X. *Int J Hydrogen Energy*, 2020, 45: 22921–22928
24 Chen W, Wu B, Wang Y, Zhou W, Li Y, Liu T, Xie C, Xu L, Du S, Song M, Wang D, liu Y, Li Y, Liu J, Zou Y, Chen R, Chen C, Zheng J, Li Y, Chen J, Wang S. *Energy Environ Sci*, 2021, 14: 6428–6440
25 Hao P, Xin Y, Tian J, Li L, Xie J, Lei F, Tong L, Liu H, Tang B. *Sci China Chem*, 2020, 63: 1030–1039
26 Lu J, Deng PJ, Chen A, Yang C, Zhu H, Liang HP. *J Mater Chem A*, 2023, 11: 2452–2459
27 Dünnwald J, Otto A. *Corrosion Sci*, 1989, 29: 1167–1176
28 Rubim JC. *J Chem Soc Faraday Trans 1*, 1989, 85: 4247–4258
29 Rémazeilles C, Refait P. *Corrosion Sci*, 2007, 49: 844–857
30 Liao H, Luo T, Tan P, Chen K, Lu L, Liu Y, Liu M, Pan J. *Adv Funct Mater*, 2021, 31: 2102772
31 Louie MW, Bell AT. *J Am Chem Soc*, 2013, 135: 12329–12337
32 Zhang Y, Su Y, Zhou X, Dai C, Keller AA. *J Hazard Mater*, 2013, 263: 685–693
33 Samide A, Tutunaru B, Negrila C, Prunaru I. *Spectr Lett*, 2012, 45: 55–64
34 Li W, Li F, Zhao Y, Liu C, Li Y, Yang H, Fan K, Zhang P, Shan Y, Sun L. *Sci China Chem*, 2022, 65: 382–390
35 Zhu Y, Wang X, Shi J, Gan L, Huang B, Tao L, Wang S. *Sci China Chem*, 2022, 65: 1445–1452

36 Yang H, Gao S, Rao D, Zhang C, Zhou X, Yang S, Ye J, Yang S, Lai F, Yan X. *Sci China Chem*, 2021, 64: 101–108
37 Chen H, Zou Y, Li J, Zhang K, Xia Y, Hui B, Yang D. *Appl Catal B-Environ*, 2021, 293: 120215
38 Cui B, Hu Z, Liu C, Liu S, Chen F, Hu S, Zhang J, Zhou W, Deng Y, Qin Z, Wu Z, Chen Y, Cui L, Hu W. *Nano Res*, 2021, 14: 1149–1155
39 Li Y, Wu X, Wang J, Wei H, Zhang S, Zhu S, Li Z, Wu S, Jiang H, Liang Y. *Electrochim Acta*, 2021, 390: 138833
40 Yu L, Wu L, McElhenny B, Song S, Luo D, Zhang F, Yu Y, Chen S, Ren Z. *Energy Environ Sci*, 2020, 13: 3439–3446
41 Yu L, Zhu Q, Song S, McElhenny B, Wang D, Wu C, Qin Z, Bao J, Yu Y, Chen S, Ren Z. *Nat Commun*, 2019, 10: 5106
42 Kang X, Yang F, Zhang Z, Liu H, Ge S, Hu S, Li S, Luo Y, Yu Q, Liu Z, Wang Q, Ren W, Sun C, Cheng HM, Liu B. *Nat Commun*, 2023, 14: 3607
43 Kloprogge JT, Wharton D, Hickey L, Frost RL. *Am Miner*, 2002, 87: 623–629
44 Tomikawa K, Kanno H. *J Phys Chem A*, 1998, 102: 6082–6088
45 Frost RL, Henry DA, Erickson K. *J Raman Spectrosc*, 2004, 35: 255–260
46 Frost RL, Čejka J, Ayoko GA, Dickfos MJ. *J Raman Spectrosc*, 2008, 39: 374–379
47 Li H, Ma J, Evans DG, Zhou T, Li F, Duan X. *Chem Mater*, 2006, 18: 4405–4414
48 Zhang Y, Lim YV, Huang S, Pam ME, Wang Y, Ang LK, Shi Y, Yang HY. *Small*, 2018, 14: 1800898
49 Debnath B, Parvin S, Dixit H, Bhattacharyya S. *ChemSusChem*, 2020, 13: 3875–3886
50 Wang Y, Yu W, Zhou B, Xiao W, Wang J, Wang X, Xu G, Li B, Li Z, Wu Z, Wang L. *J Mater Chem A*, 2022, 11: 1886–1893
51 Chen H, Zhang S, Liu Q, Yu P, Luo J, Hu G, Liu X. *InOrg Chem Commun*, 2022, 146: 110170